

TWO LENSED LYMAN- α EMITTING GALAXIES AT $z \sim 5$

MATTHEW BAYLISS^{1,2}, EVA WUYTS^{1,2}, KEREN SHARON², JOSEPH F. HENNAWI³, MICHAEL D. GLADDERS^{1,2}, BENJAMIN P. KOESTER^{1,2}

Draft version April 19, 2019

ABSTRACT

We present observations of two strongly lensed $z \gtrsim 5$ Lyman- α Emitting (LAE) galaxies that were discovered in the Sloan Giant Arcs Survey (SGAS). We identify the two sources as SGAS J091531+382655, at $z = 5.200$, and SGAS J134331+415455 at $z = 4.994$, and measure their Vega magnitudes at $(i, z) = (22.92 \pm 0.09, 22.75 \pm 0.13)$ mags and $(i, z) = (23.36 \pm 0.18, 23.70^{+0.18}_{-0.16})$ mags, respectively. Each source is strongly lensed by a massive galaxy cluster in the foreground, and the magnifications due to gravitational lensing are recovered from strong lens modeling of the foreground lensing potentials. We use the magnification to calculate the intrinsic, unlensed Lyman- α luminosities for both sources, as well as the star formation rate (SFR) implied by the Lyman- α emission. Comparison of the spectral energy distributions (SEDs) of both sources against stellar population models produce estimates of the stellar mass in each galaxy: $M_{\text{stars}} = 1.29^{+0.95}_{-0.55} \times 10^8 M_{\odot} h_{0.7}^{-1}$ for SGAS J091531+382655 and $M_{\text{stars}} \sim 6 \times 10^7 M_{\odot} h_{0.7}^{-1}$ for SGAS J134331+415455. Compared to samples of LAEs in the literature at similar redshifts, the intrinsic $L_{\text{Ly}-\alpha}$ of these two lensed sources places them well down the faint end of the luminosity function.

Subject headings: galaxies: high-redshift galaxies

1. INTRODUCTION

Understanding the evolution of galaxies – especially the first generation of galaxies – remains one of the most important topics in astrophysics and cosmology. Current efforts to study the properties of galaxies at high redshift rely on two distinct samples: 1) Lyman-Break Galaxies (LBGs) and 2) Lyman- α Emitters (LAEs). LBGs are selected via deep wide-band photometry, identified by the ‘Lyman limit’ continuum break that appears at 912\AA in the rest frame (Steidel et al. 1996a,b; Lowenthal et al. 1997) – though for sources at higher redshift this spectral break moves redward, approaching 1216\AA in the rest frame due to the Lyman- α forest (Steidel & Sargent 1987; Rauch 1998) absorption by intergalactic neutral hydrogen. LAEs are selected by either narrow-band imaging (Cowie & Hu 1998; Rhoads et al. 2000, 2003; Ajiki et al. 2004; Gawiser et al. 2006; Yamada et al. 2005) or blind spectroscopy (Kurk et al. 2004; Sawicki et al. 2008) tuned to detect Lyman- α line emission redshifted into the optical. Over the past decade large samples of LBGs and LAEs have driven studies of star-forming galaxies at $z \gtrsim 2.5$.

Surveys for LBGs and LAEs are efficient for collecting statistical samples of high-redshift galaxies, but at $z \gtrsim 3$ they produce objects which are generally too faint to be studied individually. The standard approach for studying the properties of these galaxy samples relies on stacking the photometric signal from many objects and fitting the observed mean SED against a va-

riety of stellar population synthesis models in order to constrain parameters such as the ages and masses of the underlying stellar populations (Shapley et al. 2003; Chary et al. 2005; Pirzkal et al. 2007; Lai et al. 2007; Finkelstein et al. 2008, 2009a; Nilsson et al. 2009; Yabe et al. 2009). In principal, stellar population synthesis modeling also provides information about dust content and metallicity, but even the stacked SED signal at $z \gtrsim 3$ is insufficient to constrain these additional parameters with much confidence. Broadly speaking, galaxies selected as LBGs are believed to sample more massive star-forming galaxies with an underlying older stellar population, and possibly higher dust content, while LAE selected galaxies tend to be lower mass galaxies with low metallicities and very little dust (Giavalisco 2002; Venemans et al. 2005; Gawiser et al. 2007). Hubble Space Telescope imaging studies of high redshift LAE galaxies imply that these sources are compact, and likely either disk-like or irregular in structure (Pirzkal et al. 2007; Taniguchi et al. 2009). Recently Finkelstein et al. (2009b) modeled individual SEDs of 14 bright $z \sim 4.5$ LAEs from the Chandra Deep Field South and found a broad range in stellar population age, stellar mass, and dust extinction, which suggests that stacking SED analyses of high redshift galaxies may not be the best approach.

The main hurdle involved in studying any high redshift source is the general lack of signal. Distant galaxies are faint and therefore difficult to detect, and those which are identified are rarely – if ever – amenable to aggressive follow-up. Furthermore, those sources which are bright enough to be studied individually are drawn from the extreme bright tail of the luminosity function of high redshift galaxies, and are therefore not necessarily representative of the bulk of the LBG and LAE populations. In this paper we present two serendipitously discovered, strongly lensed high redshift galaxies:

¹ Department of Astronomy & Astrophysics, University of Chicago, 5640 South Ellis Avenue, Chicago, IL 60637

² Kavli Institute for Cosmological Physics, University of Chicago, 5640 South Ellis Avenue, Chicago, IL 60637

³ Max-Planck-Institut für Astronomie Königstuhl 17, D-69117, Heidelberg, Germany

SGAS J091541+382655, spectroscopically confirmed at $z = 5.200 \pm 0.001$, with $i = 22.92 \pm 0.09$ mags and $z = 22.75 \pm 0.13$ mags, and SGAS J134330+415455 spectroscopically confirmed at $z = 4.994 \pm 0.001$, with $i = 23.36 \pm 0.18$ mags and $z = 23.70^{+0.18}_{-0.16}$ mags. At $z \gtrsim 5$ these objects are the two brightest LAEs in the literature to date, and both sources are projected on the sky within $30''$ of the cores of confirmed strong lensing galaxy clusters. This means that the sources – once corrected for the lensing magnification – are intrinsically much fainter than the observed flux implies, and therefore provide a rare opportunity to study individual LAE properties at the fainter end of the luminosity function. Throughout this paper we calculate cosmological distances assuming a flat cosmology with $H_0 = 70 \text{ km s}^{-1} \text{ Mpc}^{-1}$, and matter density $\Omega_M = 0.3$.

2. OBSERVATIONS

2.1. Data

The two sources presented here were first identified as r -band dropouts in gri imaging of two different strong lensing galaxy clusters, and subsequently confirmed by spectroscopy to have strong Lyman- α emission features. The two galaxy clusters were identified as part of the Sloan Giant Arcs Survey (SGAS; Hennawi et al. 2008), a blind survey for strong lensing systems in optically selected massive clusters at $0.1 \leq z \leq 0.6$ detected via the Red-Sequence Cluster algorithm (Gladders & Yee 2000) adapted to run on the Sloan Digital Sky Survey (SDSS; York et al. 2000) public data release catalogs. Strong lensing clusters are identified by visual inspection of imaging in g -band on 2m to 4m-class telescopes for 600s in $< 1''$ seeing, and the most spectacular systems have been followed-up with multi-band imaging and spectroscopy on 8m-class telescopes. One of the clusters discussed here, SDSSJ1343+4155, appears in a recent small sample of strong lensing clusters discovered in the SDSS by Diehl et al. (2009). The other cluster, SDSSJ0915+3826, does not appear in any prior published work. Imaging and spectroscopic observations were conducted with the Frederick C. Gillett Telescope (Gemini North) between the months of 2008 February and 2008 July. The GMOS imaging observations were pre-imaging conducted for the purpose of spectroscopic mask design. The primary goal of the spectroscopic observations was to obtain redshifts of arcs to facilitate strong lensing modeling. We briefly summarize the spectroscopy here, and refer the reader to Bayliss et al. (2010), in preparation, for additional details.

Gemini North/GMOS gri photometry for both cluster fields are derived from 2×150 s dithered exposures, which were executed in queue mode on February and March of 2008. These pre-imaging data were used for spectroscopic mask design and target prioritization. GMOS z -band observations consisted of 6×180 s dithered exposures which were scheduled as follow-up, primarily in order to measure the continuum flux of the LAEs, and were executed in queue mode in February of 2010. The GMOS images were reduced using the Gemini IRAF⁴ package.

⁴ IRAF (Image Reduction and Analysis Facility) is distributed by the National Optical Astronomy Observatories, which are operated by AURA, Inc., under cooperative agreement with the National Science Foundation.

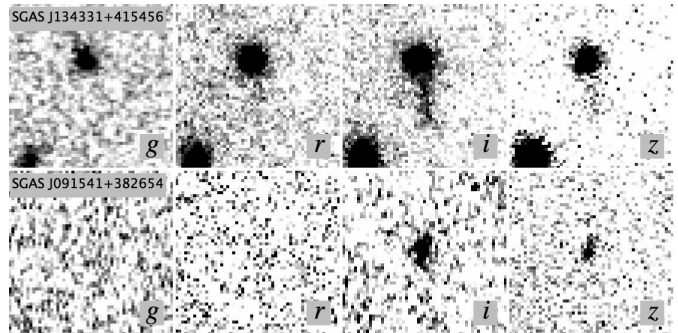


FIG. 1.— GMOS gri (from left to right) $8'' \times 8''$ cutout images centered on SGAS J091541+382654 and SGAS J134331+415455. Both objects exhibit obvious drop-out behavior from the i - to r -bands. The z -band detection of SGAS J091541+382654 appears at lower significance than its counterpart for SGAS J134331+415455 because its z data were taken during bright time and the sky background noise is $\sim 30\%$ higher.

In addition to the GMOS-N photometry and spectroscopy, we obtained near-infrared (NIR) imaging of the two lensing clusters in the $z'JH$ filters with the Near-Infrared Camera and Fabry-Perot Spectrometer (NIC-FPS) of the 3.5m telescope at the Apache Point Observatory (APO) in New Mexico. The detector is a Rockwell Hawaii 1-RG 1024x1024 HgCdTe device with a pixel scale of $0.273'' \text{ pixel}^{-1}$ and 4.58×4.58 arcmin unvignetted field of view. The APO/NIC-FPS z' data differs from the Gemini/GMOS z significantly due to the different wavelength responses of the NIC-FPS and GMOS detectors. The effective wavelengths of the two filters are offset by $\sim 1000\text{\AA}$, and we use the prime ($'$) throughout this paper to distinguish the APO/NIC-FPS z' from the Gemini/GMOS z . The NIR data were taken on 3 different nights in the Winter and Spring of 2009. The conditions during the observing nights varied, with sub-arcsecond seeing for the SDSSJ1343+4155 z' -band and both J -band images. The SDSSJ0915+3826 z' -band and both H -band images were taken in $\sim 2''$ seeing. The observations consisted of 5-point dithers around a $40''$ box and were reduced, registered and stacked using a custom IRAF pipeline. Total exposure times are 5400s, 6960s and 3500s for z' -, J -, and H -band observations of SDSSJ0915+3826 and 7800s, 5160s and 2625s for z' -, J -, and H -band observations of SDSSJ1343+4155.

The SDSS is used to calibrate the four optical bands and the Two Micron All Sky Survey (2MASS) is used to calibrate the NIR observations. Prior to making any photometric measurements we first transform images in all bands to the reference frame of the i -band image, $0.1454'' \text{ pixel}^{-1}$ (GMOS-North detector, binned 2×2). We then construct an empirical, normalized point spread function (PSF) for each image based on a well-defined, non-saturated reference star. We create photometric apertures by drawing a ridge line that covers the high-redshift LAE and convolving it with the appropriate PSF for each image. Apertures are defined by an equivalent radius, which corresponds to the radius of a circular aperture that goes out to the same PSF level. We make the final magnitude measurement using a detailed sequence of sky subtraction and out-lier masking steps; first we subtract a general sky measurement and then compute the median pixel value and standard deviation inside annuli of fixed width at increasing radial distances from the source. Far

enough out, these median values converge to zero for an accurate sky subtraction. We average the median values at large radii and subtract this average from the image to correct the general sky subtraction. Outliers are defined as pixel values that deviate by more than 5σ from the median in the respective annuli, and are replaced by the median value plus an appropriate noise term. The final magnitude is measured at an equivalent radius of twice the FWHM of the image and corrected to an equivalent radius of $6''$ based on the curve of growth of the psf-star. By defining the radius as twice the FWHM, we make sure our apertures always cover the same physical region on the sky. In the case of SGAS J091541+382655, a foreground galaxy lies very close to and partially on top of the LAE galaxy. We use the **GALFIT** package (Peng et al. 2002) to fit a Sérsic profile to this galaxy in each band and subtract out its flux.

When the LAEs are not detected (in *gJH* for SGAS J091541+382655 and *grJH* for SGAS J134331+415455), we measure a limiting magnitude, derived from the total sky noise in the aperture. We define a sky noise per pixel σ_{sky} as the standard deviation of our overall sky measurement plus a contribution from the poison error made in this measurement. A pixel value of $2\sigma_{sky}$ is added in quadrature for each pixel in our final aperture with an equivalent radius equal to twice the FWHM. The limiting magnitudes are also aperture corrected to an equivalent radius of $6''$. This method constrains the source to be fainter than the limiting magnitudes at 95% confidence in the relevant bandpasses.

All spectroscopic observations were carried out using the Gemini Multi-Object Spectrograph (Hook et al. 2004) using custom slitmasks that were designed to target lensed sources based on their color and morphology in the GMOS imaging. After targeting all of the arc candidates, any remaining slits were placed on cluster members, easily identified by their red sequence colors. Spectra were taken using the macroscopic nod-and-shuffle (N&S) mode available on GMOS. The reasons for using N&S are threefold. First, many of the emission or absorption features that are used to determine galaxy redshifts in the range $z = 1.0 - 3.0$ characteristic of the giant arcs, are in the redder part of the optical where sky lines are problematic, and N&S facilitates more accurate sky-subtraction (Glazebrook & Bland-Hawthorn 2001), particularly at low-spectral resolution. Second, N&S sky-subtraction allows us to use very small $1'' \times 1''$ microslits that can be densely packed into the cluster core ($\sim 30''$), allowing us to target as many arcs, arclets, and cluster galaxies as possible (Gilbank et al. 2008). Third, as we are primarily interested in a number of objects around the cluster center, the density of objects and the limited field of interest are perfect for block-shuffling N&S observations. Spectra were taken with the R150_G5306 grating in first order which gives a dispersion of 3.5\AA per pixel (binned spectrally by two), with six pixels per resolution element resulting in a spectral FWHM $\simeq 940 \text{ km s}^{-1}$. Although the R150 grating offers broad spectral range from the atmospheric cutoff to $\lambda \gtrsim 1\mu\text{m}$, the drop in sensitivity at the blue and red extremes, due both to the GMOS CCD and the R150 grating efficiency, results in effective spectral coverage of $\sim 4000 - 9500\text{\AA}$.

The N&S technique employed in our program is non-standard in that it involves a nod distance on the sky that is $1/2$ the size of the macroscopic shuffle. The mask is designed to incorporate two submasks, each of which is a set of slits covering an area $1/3$ the size of the detector. Slits for the two submasks overlap on the sky in an area that is $1/6$ the size of the detector (because the nod distance is set to half the shuffle distance). This design allows us to place science slits for the primary target – the core of a strong lensing cluster in this case – on both submasks and obtain useful spectra for the entire duration of the N&S exposure, whereas standard macroscopic N&S results in science spectra for only $1/2$ the total exposure time. Our integration times were 2400s resulting in a 1200s effective integration for each of the two submasks. Two exposures were taken for each target. Thus if an arc was targeted on both submasks (typical for the most prominent arcs) the total integration time was 4800s. N&S facilitates straightforward sky subtraction by differencing two sections of the detector – each $1/3$ the size of the full detector. The spectra presented here were wavelength calibrated, stacked, extracted and analyzed using a custom pipeline based on the XIDL software package⁵.

2.2. SGAS J091541+382655

SDSSJ0915+3826 is a new strong lensing cluster that was discovered in the SGAS – discussed above. Combining our Gemini/GMOS spectroscopy with a redshift for the BCG measured in the SDSS we measure a mean cluster redshift of $z = 0.395$ and a velocity dispersion of $999 \pm 140 \text{ km s}^{-1}$ from 13 cluster member galaxies. The most prominent strong lensing feature around this cluster is a spectroscopically confirmed background galaxy at $z = 1.501$. Pre-imaging of this cluster revealed a source near the cluster core that exhibited a dramatic drop in flux from the *i*- to *r*-band, as shown in Figure 1. With Gemini/GMOS-N, in *griz*, we measure this source at $g \geq 26.15$ mags, $r=24.68 \pm 0.25$ mags, $i=22.92 \pm 0.09$ mags, and $z=22.75 \pm 0.13$ mags. Slits were placed on this source in both submasks for our N&S observation of this cluster and the spectra exhibit bright emission at 7539\AA which we interpret as Lyman- α $\lambda 1216\text{\AA}$ at $z = 5.200$.

The LAE galaxy in this case is located on the sky very near to a foreground galaxy, and so we took care to account for possible contamination in the LAE spectrum by light from the galaxy that falls into the slit, as this could mimic a continuum break in the source spectrum. The separation between the LAE box slit and the potentially contaminating foreground galaxy is $2.5''$. Examination of the radial profile of the potential contaminant in the pre-imaging observation shows that the *i*-band flux within the LAE slit due to the galaxy is on average 1.5×10^{-3} of the peak flux of that galaxy. The mean *i*-band flux of the LAE within the spectroscopic aperture is 5.1×10^{-2} compared to the peak of the contaminating galaxy, and thus assuming comparable seeing between the imaging and spectroscopic observations suggests that this object's contribution to the *i*-band flux within the LAE aperture is approximately 3% of the total

⁵ <http://www.ucolick.org/~xavier/IDL/index.html>

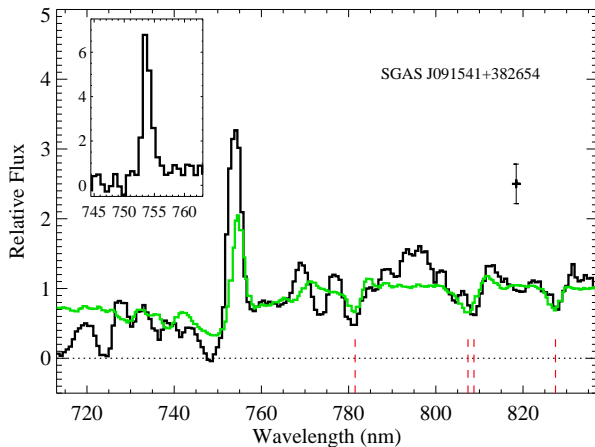


FIG. 2.— GMOS spectrum of the Lyman- α emitter behind cluster lens SDSSJ0915+3826. The LAE spectrum plotted over a range of $\sim 7150 - 8350\text{\AA}$ is smoothed with a kernel of $3\times$ the spectral resolution of the data, with the composite Lyman Break Galaxy absorption+emission spectrum from Shapley et al. (2003) overplotted in green. Dashed vertical lines indicate the location of prominent UV continuum metal absorption lines at the LAE redshift, which coincide with low-significance features in our continuum spectrum. The Lyman- α emission feature is shown inset, unsmoothed.

light. Note that given the separation between the contaminant and the slit the seeing of the spectroscopic and imaging observations would have to be grossly different to produce significant contamination; such a mismatch is neither expected due to execution of the observations in specified conditions in queue mode, nor suggested by the spatial width of stellar spectra within the alignment boxes of the spectroscopic observations.

The relevant part of the extracted spectrum is displayed in Figure 2, and despite the low dispersion grating used for our observations the line is measurably asymmetric. We also detect continuum signal redward of the emission line and no significant signal blueward of it. This source has a dramatic photometric r - i break – even after subtracting the emission line flux from the i -band photometry, is also very blue in i - z , and is not detected in NIC-FIPS imaging to $2\text{-}\sigma$ limiting magnitudes of $z' \geq 21.87$ mags, $J \geq 21.55$ mags, and $H \geq 19.51$ mags, all of which indicates that the continuum spectral slope redward of the emission feature is blue. The blue continuum redward of the emission and the strong r - i break – along with the non-detection in g , and the asymmetry of the line confirm the interpretation of the source as a Lyman- α emitting galaxy at high redshift. At $z = 5.200$ we measure a rest-frame equivalent width for the Lyman- α emission of $25.3 \pm 4.1\text{\AA}$, and an observed Lyman- α line flux of $1.15 \pm 0.21 \times 10^{-16} \text{ ergs s}^{-1} \text{ cm}^{-2}$.

2.3. SGAS J134331+415455

The second lensed LAE presented here is located near the strong lensing cluster SDSSJ1343+4155, which was published by Diehl et al. (2009) as one of four bright arcs discovered from in the SDSS. We combine our Gemini/GMOS spectroscopy with two cluster member redshifts from the SDSS to measure a mean cluster redshift of $z = 0.421$ and a velocity dispersion of $874 \pm 288 \text{ km s}^{-1}$ from 7 cluster member galaxies. The bright arc around this lens is spectroscopically confirmed as a background

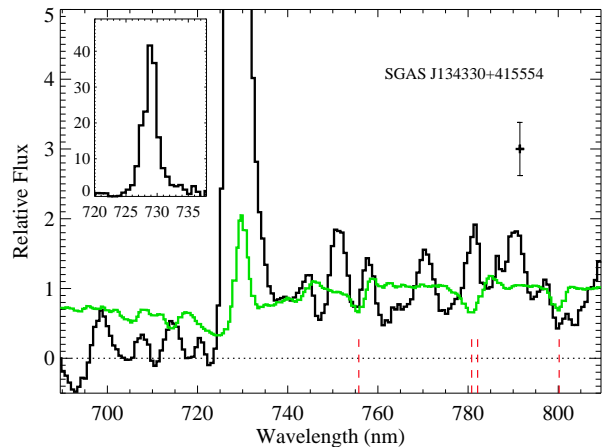


FIG. 3.— GMOS spectrum of the Lyman- α emitter behind cluster lens SDSSJ1343+4155. The LAE spectrum plotted over a range of $\sim 6900 - 8100\text{\AA}$ is smoothed with a kernel of $3\times$ the spectral resolution. Dashed vertical lines and the spectrum overplotted in green are the same as in Figure 2. The Lyman- α emission feature is shown inset, unsmoothed.

galaxy at $z = 2.091$. Pre-imaging of this cluster reveals a source near the cluster core that exhibits a dramatic drop in flux from the i - to r -band – shown in Figure 1. We measure this source at $g \geq 26.05$ mags, $r \geq 25.47$ mags, $i = 23.36 \pm 0.12$ mags, and $z = 23.7^{+0.18}_{-0.16}$ mags. We placed slits on this source in each of the two submasks for our spectroscopic N&S observations of this cluster. The spectra corresponding to these slits exhibit a bright emission line at 7289\AA , which we interpret as Lyman- α $\lambda 1216\text{\AA}$ at $z = 4.994$.

The extracted spectrum around the emission feature is displayed in Figure 3. The emission feature is significantly asymmetric and we measure continuum emission redward of the line, but no continuum blueward. The source is undetected in NIC-FIPS imaging down to $2 - \sigma$ limiting magnitudes of $z' \geq 22.77$ mags, $J \geq 21.28$ mags, and $H \geq 19.44$ mags. Similarly to the case of SGAS J091541+382655, this source has a very blue i - z color and our NIR photometry implies that it has a blue continuum spectral slope redward of the emission feature. However, this source is fainter than SGAS J091541+382655 and after subtracting the Lyman- α line emission from the i -band our photometry is insufficient to measure a large enough r - i color to make the Lyman- α interpretation trivial. The most likely candidate emission lines which could be misinterpreted as Lyman- α in this spectrum are O[II] $\lambda 3727\text{\AA}$ and MgII $\lambda 2800\text{\AA}$ – each of which can also be accompanied by a nearby spectral break – but we rule out these two potential interpretations based on the absence of other features that would accompany these two lines. Interpreting the line as O[II] $\lambda 3727\text{\AA}$ would imply a redshift of $z = 0.956$, placing H β $\lambda 4862\text{\AA}$ and O[III] $\lambda 4960, 5007\text{\AA}$ just within the spectral range covered by our data. Similarly, interpreting the line as MgII $\lambda 2800\text{\AA}$ would imply that the source is a quasar at a redshift of 1.603, for which we would expect a much broader emission feature with a lower equivalent width ($z = 1.6$ implies a rest-frame equivalent width of 312\AA), as well as a spectral break that does not coincide precisely with the emission feature. Taking the source redshift as $z = 4.994$

we measure a rest-frame equivalent width for the Lyman- α emission of $135.6 \pm 20.3 \text{ \AA}$ and an observed Lyman- α line flux of $1.50 \pm 0.24 \times 10^{-16} \text{ ergs s}^{-1} \text{ cm}^{-2}$.

3. ANALYSIS

3.1. Lens Models and Intrinsic Luminosities

Using the measured equivalent widths and i magnitudes we also calculate lensed isotropic Lyman- α line luminosities of $L_{Ly-\alpha} = 3.27 \pm 0.61 \times 10^{43} \text{ erg s}^{-1} h_{0.7}^2$ and $L_{Ly-\alpha} = 3.90 \pm 0.61 \times 10^{43} \text{ erg s}^{-1} h_{0.7}^2$ for SGAS J091541+382655 and SGAS J134331+415455, respectively. These are not the true isotropic luminosities because both sources are lensed by foreground galaxy clusters, and are therefore significantly magnified. To measure the intrinsic luminosities of the LAEs, we estimate the magnification due to strong lensing by the intervening clusters. The mass models are constructed using the publicly available software, LENSTOOL (Jullo et al. 2007), with Monte Carlo Markov Chain (MCMC) minimization in the source plane, and are shown in Figure 4. For SDSSJ1343+4155, we compute a simple mass model using as constraints the giant blue arc at $z = 2.09$, the LAE at $z = 4.994$, paired with counter-image candidate that we have identified. The cluster and the brightest cluster galaxy (BCG) are represented by pseudo isothermal elliptical mass distributions (PIEMD; Jullo et al. 2007). We allow all the parameters of the cluster halo to vary. For the BCG, we follow the light distribution for the positional parameters, and vary the core and cut radii and the velocity dispersion. Our best-fit model reproduces the locations and orientations of the observed lensed images, and is consistent with the measured velocity dispersion to within the uncertainty. Based on this model, the magnification at the location of the LAE is $m \sim 12$, which we use to calculate the intrinsic isotropic Lyman- α line luminosity for SGAS J134331+415455 to be $L_{Ly-\alpha} = 3.25 \pm 0.51 \times 10^{42} \text{ erg s}^{-1} h_{0.7}^2$. Assuming Case B recombination and taking the prescription from Kennicutt 1998 we calculate the star-formation rate (SFR) for SGAS J134331+415455 to be $\text{SFR}_{Ly-\alpha} = 2.96 \pm 0.46 M_{\odot} \text{ yr}^{-1} h_{0.7}^{-1}$. The intrinsic Lyman- α line luminosity for this source – plotted in Figure 6 – places it far down the luminosity function for LAE samples reported in the literature.

The strong lensing model for SDSSJ0915+3826 is constrained by the positions of the components of the giant arc. We do not identify a clear counter image for the LAE, and therefore do not use it as a constraint. We represent the lens with a single PIEMD and allow all its parameters to vary, except for the velocity dispersion, which we fix at the measured value, 999 km s^{-1} . The critical curves for our best-fit model are plotted in Figure 5. Since the available constraints are internal to the radial projection of the LAE, the predicted LAE magnification is highly uncertain. In particular, if we compute a set of models with parameters in the range allowed by the uncertainties, the location of the critical curve for the LAE varies significantly and there is practically no upper limit for the implied magnification. Since in all cases the magnification is higher than ~ 10 , we adopt this number as our working order-of-magnitude estimate and determine an upper limit for the intrinsic isotropic Lyman- α line luminosity for SGAS J091541+382655 of

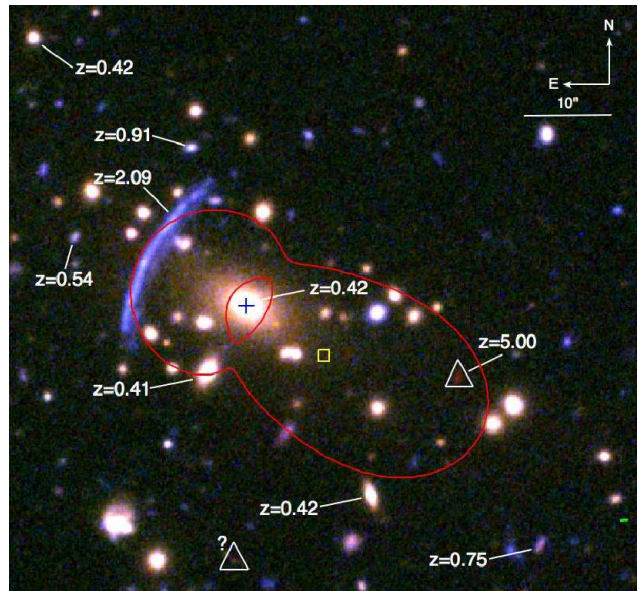


FIG. 4.— The field of SDSSJ1343+4155 with tangential and radial critical curves for the bright main arc overplotted. One image of the lensed background LAE, spectroscopically confirmed at $z = 4.994$, and its putative counterimage predicted by the lensing model are identified by white triangles. Other sources in the field – background objects and cluster members – are labeled with their spectroscopic redshifts. Color images are created from Gemini+GMOS-North gri 300s pre-imaging data.

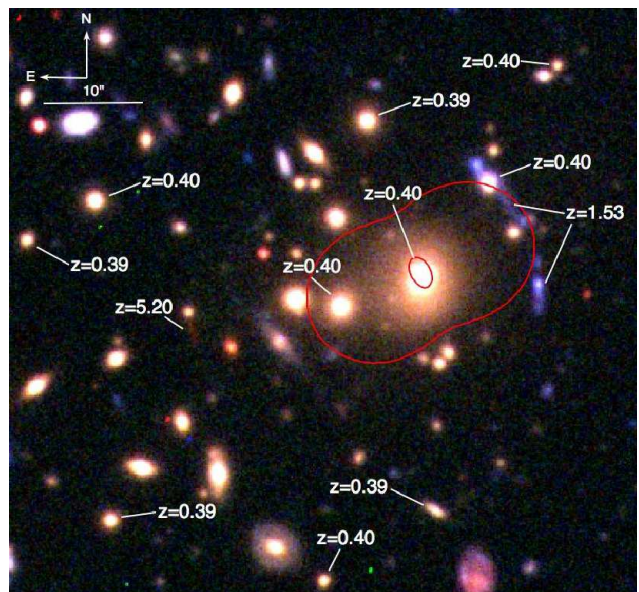


FIG. 5.— The field of SDSSJ0915+3826 with the tangential critical curve for the bright main arc overplotted. Other sources with spectroscopic redshifts are also identified, including the lensed background LAE at $z = 5.200$. Color images are created from Gemini+GMOS-North gri 300s pre-imaging data.

$L_{Ly-\alpha} \leq 3.27 \pm 0.61 \times 10^{42} \text{ ergs s}^{-1} h_{0.7}^2$ and a corresponding $\text{SFR}_{Ly-\alpha} \leq 2.97 \pm 0.55 M_{\odot} \text{ yr}^{-1} h_{0.7}^{-1}$. As with SGAS J134331+415455, the strong limit placed on the intrinsic Lyman- α line luminosity for SGAS J091541+382655 places it far down the luminosity function, as shown in (Figure 6).

Estimates of the SFR from Lyman- α luminosities for these two sources are only robust in the absence of dust extinction, but the two LAE sources presented here

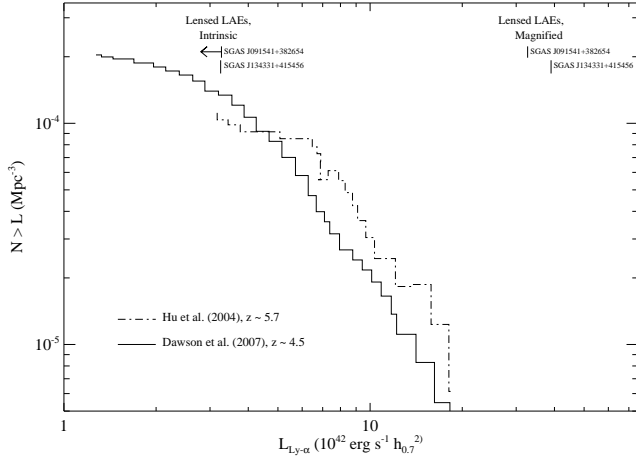


FIG. 6.— Two empirical cumulative Lyman- α line emission luminosity functions for LAEs at high redshift are plotted; a sample of $z \sim 4.5$ LAEs published by Dawson et al. (2007) is given by the solid histogram and a sample of $z \sim 5.7$ LAEs (Hu et al. 2004) by the dot-dashed histogram. Overplotted are arrows indicating both the observed, lensed luminosities for the two sources presented in this paper, and also their lensing-corrected true intrinsic luminosities. The magnification due to strong lensing of these two sources allows us to probe much fainter in the Lyman- α luminosity function but measure signal comparable to the rarest and brightest LAEs at $z \gtrsim 5$.

should have negligible spectral reddening due to dust based on our photometric data which constrains both sources to have blue UV continuum slopes. Taking into account the limited constraints that we can place on the UV continua, the star formation rates derived from Lyman- α line emission for SGAS J134331+415455 and SGAS J091541+382655 seem modest, but are in line with previous measurements of SFRs in LAEs at $z \gtrsim 5$ (Ajiki et al. 2003). Additionally, previous studies of star forming galaxies at high redshift often find that the SFR calculated from Lyman- α emission is systematically lower than other SFR metrics – such as UV continuum flux density at 1500Å – by a factor of ~ 5 or more (Tapken et al. 2007), so the SFRs calculated here should be treated as lower limits of the true SFR for these galaxies. We have also considered the possibility that the Lyman- α emission in one or both of these objects could be due all or in-part to AGN activity. Given the lack of detection of significant emission from highly ionized species, such as N[V] and C[IV], we conclude that it is unlikely that AGN are playing a significant role in the observed Lyman- α emission.

3.2. Stellar Mass and UV Continuum Properties

After accounting for the lensing magnification of the two LAEs, we compare our photometry for these sources against modified stellar population synthesis models based on those published in Bruzual & Charlot (2003), provided by the authors via private communications. We conclude that the UV continuum immediately redward of Lyman- α for SGAS J091541+382655 is constrained to originate from a young, dust-free stellar population (Figure 7). Models used here assume a solar metallicity, a Salpeter IMF (Salpeter 1955), and a reddening law derived empirically from local starburst galaxies (Calzetti 2000). The fitting is performed with an adapted version of HyperZ (Bolzonella 2000), kindly provided by M. Bolzonella, that was adapted to fit at constant

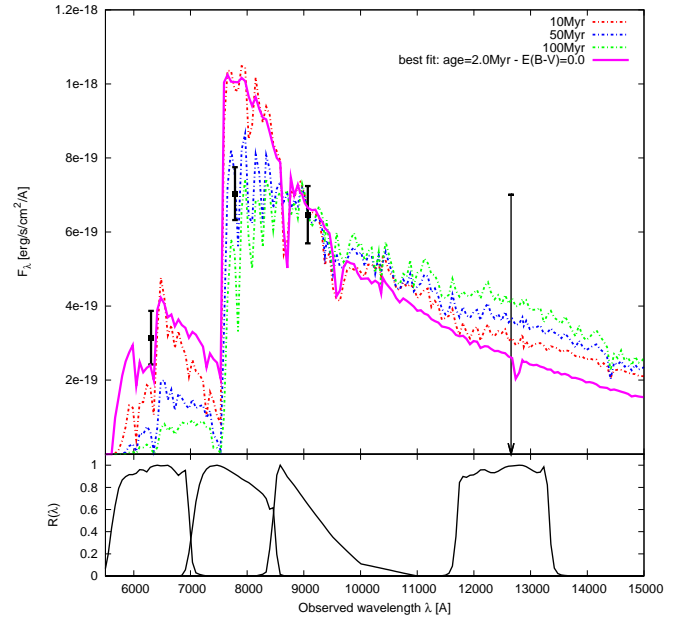


FIG. 7.— Stellar population synthesis models adapted from Bruzual and Charlot (2003) – generously provided by the authors via private communication – are plotted on top of the photometric data for SGAS J091541+382655. The solid magenta stellar population model is a fit to the LAE SED where the star formation history is unconstrained (the data have no power to distinguish between single burst and exponentially decaying SFRs). The best-fit model is a stellar population $\lesssim 5.7$ Myr old with a stellar mass of $\log_{10}(M_{\text{Stars}}) = 8.11 \pm 0.24$. Dashed-dot models are also overplotted – scaled to match the observed z-band flux – to illustrate that the data favor a young (i.e. blue) stellar populations. We lack the NIR photometric depth necessary to constrain parameters beyond a stellar mass estimate and an upper limit on the age. Filter transmission curves corresponding to the photometry are plotted in the bottom panel - r, i, z, J from left to right.

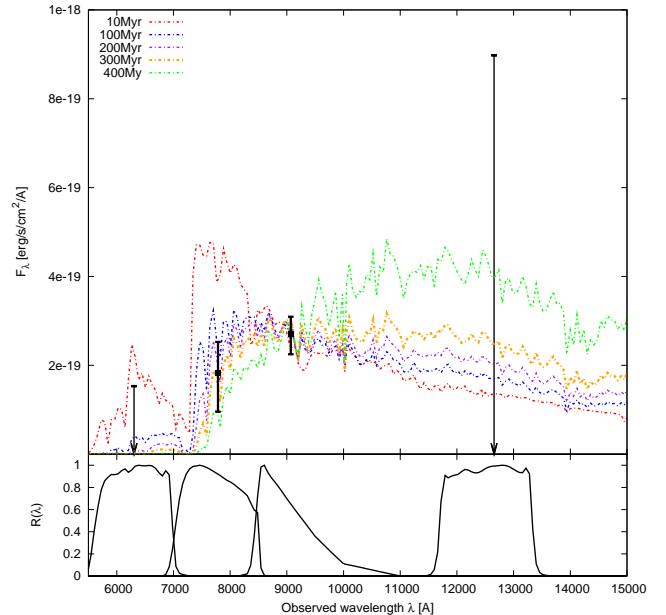


FIG. 8.— Stellar population synthesis models similar to those plotted in Figure 7 are compared against our photometry for SGAS J134331+415455. This source is the fainter of the two lensed LAEs and our photometry are not sufficient for a reliable best-fit solution. The stellar population models are all dust-free single starburst populations that are scaled to match the z-band continuum fluxes. Models with ages anywhere in the range of $10 \text{ Myr} \lesssim t_{\text{age}} \lesssim 400 \text{ Myr}$ are potentially good fits for the limited data in-hand. Filter transmission curves corresponding to the photometry are plotted in the bottom panel - r, i, z, J from left to right.

redshift. Fitting to the *grizJH* photometry for SGAS J091541+382655 we recover a best-fit model consisting of a young ($t_{age} \lesssim 5.7$ Myr) single starburst stellar population with a stellar mass $M_{stars} = 1.29^{+0.95}_{-0.55} \times 10^8 M_{\odot} h_{0.7}^{-1}$. The NIR photometry does not give us the power to constrain the properties of the young stellar populations in detail, or calculate robust UV continuum slope.

The data for SGAS J134331+415455 are insufficient to produce a robust best-fit stellar population, though we find the data are generally consistent with an underlying stellar population that is $t_{age} \lesssim 500$ Myr and dust free; the SED is plotted against several stellar population models in Figure 8. If we assume that the stars of SGAS J134331+415455 have an age comparable to those of SGAS J091541+382655 then we recover a stellar mass of $M_{stars} \sim 6 \times 10^7 M_{\odot} h_{0.7}^{-1}$. All of the available photometric data for these sources is sampling light blueward of the 4000Å break in the source frame, and therefore has no power to constrain stellar mass that may be present in the form of a large population of very old stars.

In addition to SED modeling of the photometry of both LAEs, we also take advantage of the modest continuum signal that is detected for SGAS J091541+382655. Cross correlation of our GMOS spectrum for this source over a wavelength range of 1230-1350Å (source frame) against the composite LBG spectrum from Shapley et al.(2003), which results in a peak at $z \sim 5.2$, in agreement with the redshift measured from the Lyman- α emission. The composite LBG is plotted with our GMOS spectra for both targets in Figures 2 and 3, and visual comparison of the continuum against the LBG composite spectrum suggests the presence of several strong UV metal absorption lines that are observed in well-studied LBGs and lower redshifts (e.g. Pettini et al. 2000). The features are at too low a significance in our data to claim a robust detection of individual absorption lines, but the cross correlation signal alone is surprising and encouraging given our low resolution spectra and limited integration time. Both of the sources presented here are excellent candidates for a more aggressive spectroscopic followup effort to explore the gas properties and stellar metallicity in representative low-mass starforming galaxies at $z \sim 5$.

4. SUMMARY AND CONCLUSIONS

We have identified two lensed Lyman- α emitting galaxies at $z \gtrsim 5$ near the cores of strong lensing selected galaxy clusters. These sources are among the brightest galaxies identified at such high redshift, but their intrinsic luminosities are much lower than the observed flux due to magnification by the gravitational potential of foreground galaxy clusters. We use the available data to investigate the underlying stellar populations for these galaxies and find that the light – continuum and line emission – from both sources likely originates from populations of young stars which have low dust content and have undergone or are in the process of undergoing active star formation. Modeling of both galaxies implies that we are observing star-forming galaxies that are dominated by young stellar populations with masses $M_{stars} \leq 2.25 \times 10^8 M_{\odot} h_{0.7}^{-1}$, and possibly as low as $M_{stars} \sim 6 \times 10^7 M_{\odot} h_{0.7}^{-1}$ in the case of SGAS J134331+415455. Identifying these two LAEs as low mass star forming galaxies with little or no dust corroborates our current understanding of the nature of Lyman- α emitting galaxies at high redshift, and the large magnification of these sources due to gravitational lensing makes them excellent candidates for studying the individual properties of galaxies on the faint end of the $L_{Ly-\alpha}$ luminosity function at $z \sim 5$. We encourage efforts to followup these sources aggressively on 8-10m class telescopes in order to study the properties of the underlying stellar populations via continuum light. With additional data these sources can provide an exciting new window into the physical properties of high redshift galaxies.

MBB acknowledges the support of the Sigma Xi Scientific Research Society in the form of a grant in-aid of research. We also wish to thank the Gemini North observing and support staff for their efforts in taking data that contributed to this paper. The authors wish to recognize and acknowledge the very significant cultural role and reverence that the summit of Mauna Kea has always had within the indigenous Hawaiian community. We are most fortunate to have the opportunity to conduct observations from this mountain.

REFERENCES

- Ajiki, Masaru; Taniguchi, Yoshiaki; Fujita, Shinobu S.; Shioya, Yasuhiro; Nagao, Tohru; Murayama, Takashi; Yamada, Sanae; Umeda, Kazuyoshi; Komiyama, Yutaka 2003, AJ, 126, 2091A
- Ajiki, Masaru; Taniguchi, Yoshiaki; Fujita, Shinobu S.; Shioya, Yasuhiro; Nagao, Tohru; Murayama, Takashi; Yamada, Sanae F.; Umeda, Kazuyoshi; Sasaki, Shunji S.; Sumiya, Ryoko; Komiyama, Yutaka 2004, PASJ, 56, 597A
- Bolzonella, M., Miralles, J.-M., Pelló, R. 2000, A&A, 363, 476
- Bruzual, G.; Charlot, S. 2003, MNRAS, 344, 1000B
- Calzetti, D., Armus, L., Bohlin, R. C., Kinney, A. L., Koornneef, J., Storchi-Bergmann, T. 2000, ApJ, 533, 68
- Chary, Ranga-Ram, Stern, Daniel, Eisenhardt, Peter 2005, ApJ, 635L, 5C
- Cowie, L. L. & Hu, E. M. 1998, AJ, 115, 1319
- Dawson, Steve; Rhoads, James E.; Malhotra, Sangeeta; Stern, Daniel; Wang, JunXian; Dey, Arjun; Spinrad, Hyron; Jannuzi, Buell T. 2007, ApJ, 671, 1227D
- Diehl, H. Thomas; Allam, Sahar S.; Annis, James; Buckley-Geer, Elizabeth J.; Frieman, Joshua A.; Kubik, Donna; Kubo, Jeffrey M.; Lin, Huan; Tucker, Douglas; West, Anderson 2009, ApJ, 707, 686D
- Dow-Hygelund, C. C.; Holden, B. P.; Bouwens, R. J.; Illingworth, G. D.; van der Wel, A.; Franx, M.; van Dokkum, P. G.; Ford, H.; Rosati, P.; Magee, D.; Zirm, A. 2007, ApJ, 660, 47D
- Finkelstein, Steven L.; Rhoads, James E.; Malhotra, Sangeeta; Grogin, Norman; Wang, Junxian 2008, ApJ, 678, 655F
- Finkelstein, Steven L., Papovich, Casey, Giavalisco, Mauro, Redd, Naveen A., Ferguson, Henry C., Koekemoer, Anton M.; Dickinson, Mark 2009, arXiv0912.1338F
- Finkelstein, Steven L., Rhoads, James E., Malhotra, Sangeeta, Grogin, Norman 2009, ApJ, 691, 465F

- Gawiser, Eric; van Dokkum, Pieter G.; Gronwall, Caryl; Ciardullo, Robin; Blanc, Guillermo A.; Castander, Francisco J.; Feldmeier, John; Francke, Harold; Franx, Marijn; Habertzettl, Lutz; Herrera, David; Hickey, Thomas; Infante, Leopoldo; Lira, Paulina; Maza, José; Quadri, Ryan; Richardson, Alexander; Schawinski, Kevin; Schirmer, Mischa; Taylor, Edward N.; Treister, Ezequiel; Urry, C. Megan; Virani, Shanil N. 2006, *ApJ*, 642L, 13G
- Gawiser, Eric; Francke, Harold; Lai, Kamson; Schawinski, Kevin; Gronwall, Caryl; Ciardullo, Robin; Quadri, Ryan; Orsi, Alvaro; Barrientos, L. Felipe; Blanc, Guillermo A.; Fazio, Giovanni; Feldmeier, John J.; Huang, Jia-sheng; Infante, Leopoldo; Lira, Paulina; Padilla, Nelson; Taylor, Edward N.; Treister, Ezequiel; Urry, C. Megan; van Dokkum, Pieter G.; Virani, Shanil N. 2007, *ApJ*, 671, 278G
- Mauro Giavalisco *AARA&A*, 2002, 40, 579
- Gilbank, David G., Yee, H. K. C., Ellingson, E., Hicks, A. K., Gladders, M. D., Barrientos, L. F., Keeney, B. 2008, *ApJ*, 677L, 89G
- Gladders, M. D. and Yee, H. K. C. 2000, *AJ*, 120, 2148G
- Karl Glazebrook & Joss Bland-Hawthorn 2001, *PASP*, 113, 197G
- Hennawi et al. 2008, *AJ*, 135, 664H
- Hook, Isobel; Jrgensen, Inger; Allington-Smith, J. R.; Davies, R. L.; Metcalfe, N.; Murowinski, R. G.; Crampton, D., 2004, *PASP*, 116, 425
- Hu, Esther M.; Cowie, Lennox L.; Capak, Peter; McMahon, Richard G.; Hayashino, Tomoki; Komiyama, Yutaka 2004, *AJ*, 127, 563H
- Jullo, E.; Kneib, J.-P.; Limousin, M.; Elasdttir, .; Marshall, P. J.; Verdugo, T. 2007, *NJPh*, 9, 447J
- Robert C. Kennicutt Jr. 1998, *ARA&A*, 36, 189K
- Kurk, J. D., Cimatti, A., di Serego Alighieri, S., Vernet, J., Daddi, E., Ferrara, A., Ciardi, B. 2004, *A&A*, 422L, 13K
- Lai, Kamson; Huang, Jia-Sheng; Fazio, Giovanni; Cowie, Lennox L.; Hu, Esther M.; Kakazu, Yuko 2007, *ApJ*, 655, 704L
- Lowenthal, James D.; Koo, David C.; Guzman, Rafael; Gallego, Jesus; Phillips, Andrew C.; Faber, S. M.; Vogt, Nicole P.; Illingworth, Garth D.; Gronwall, Caryl. 1997, *ApJ*, 481, 673L
- Nilsson, K. K.; Tapken, C.; Mller, P.; Freudling, W.; Fynbo, J. P. U.; Meisenheimer, K.; Laursen, P.; Östlin, G. 2009, *A&A*, 498, 13N
- Peng, C. Y., Ho, L. C., Impey, C. D., Rix, H.-W. 2002, *AJ*, 124, 266
- Pettini, Max; Steidel, Charles C.; Adelberger, Kurt L.; Dickinson, Mark; Giavalisco, Mauro 2000, *ApJ*, 528, 96P
- Pirzkal, N.; Malhotra, S.; Rhoads, J. E.; Xu, C. 2007, *ApJ*, 667, 49P
- Rauch, Michael *ARA&A*, 1998, 36, 267
- Riediger, Rudiger; Petitjean, Patrick; Mucket, Jan P. 1998, *A&A*, 329, 30R
- Rhoads, J. E.; Malhotra, S.; Dey, A.; Stern, D.; Spinrad, Jannuzi, B. T. 2000, *ApJ*, 545L, 85R
- Rhoads, J. E.; Dey, Arjun; Malhotra, Sangeeta; Stern, Daniel; Spinrad, Hyron; Jannuzi, Buell T.; Dawson, Steve; Brown, Michael J. I.; Landes, Emily 2003, *AJ*, 125, 1006R
- Salpeter, E. E. 1955, *ApJ*, 121, 161
- Sawicki, Marcin; Lemaux, Brian C.; Guhathakurta, Puragra; Kirby, Evan; Konidaris, Nicholas P.; Martin, Crystal L.; Cooper, Michael C.; Koo, David C.; Newman, Jeffrey A.; Weiner, Benjamin J. 2008, *ApJ*, 687, 884S
- Shapley, Alice; Steidel, Charles; Pettini, Max; Adelberger, Kurt L. 2003, *ApJ*, 588, 65
- Shioya, Y.; Taniguchi, Y.; Sasaki, S. S.; Nagao, T.; Murayama, T.; Saito, T.; Ideue, Y.; Nakajima, A.; Matsuoka, K.; Trump, J.; Scoville, N. Z.; Sanders, D. B.; Mobasher, B.; Aussel, H.; Capak, P.; Kartaltepe, J.; Koekemoer, A.; Carilli, C.; Ellis, R. S.; Garilli, B.; Giavalisco, M.; Kitzbichler, M. G.; Impey, C.; LeFevre, O.; Schinnerer, E.; Smolcic, V. 2009, *ApJ*, 696, 546S
- Steidel, Charles C.; Sargent, Wallace L. W. 1987, *ApJ*, 313, 171S
- Steidel, Charles C.; Giavalisco, Mauro; Dickinson, Mark; Adelberger, Kurt L. 1996, *AJ*, 112, 352S
- Steidel, Charles C.; Giavalisco, Mauro; Pettini, Max; Dickinson, Mark; Adelberger, Kurt L. 1996, *ApJ*, 462L, 17S
- Taniguchi, Y.; Murayama, T.; Scoville, N. Z.; Sasaki, S. S.; Nagao, T.; Shioya, Y.; Saito, T.; Ideue, Y.; Nakajima, A.; Matsuoka, K.; Sanders, D. B.; Mobasher, B.; Aussel, H.; Capak, P.; Salvato, M.; Koekemoer, A.; Carilli, C.; Cimatti, A.; Ellis, R. S.; Garilli, B.; Giavalisco, M.; Ilbert, O.; Impey, C. D.; Kitzbichler, M. G.; LeFevre, O.; McCracken, H. J.; Scarlata, C.; Schinnerer, E.; Smolcic, V.; Tribiano, S.; Trump, J. R. 2009, *ApJ*, 701, 915T
- Tapken, C.; Appenzeller, I.; Noll, S.; Richling, S.; Heidt, J.; Meinköhn, E.; Mehlert, D. 2007, *A&A*, 467, 63T
- Venemans, B. P.; Röttgering, H. J. A.; Miley, G. K.; Kurk, J. D.; De Breuck, C.; Overzier, R. A.; van Breugel, W. J. M.; Carilli, C. L.; Ford, H.; Heckman, T.; Pentericci, L.; McCarthy, P. 2005, *A&A*, 431, 793V
- Yabe, Kiyoto; Ohta, Kouji; Iwata, Ikuru; Sawicki, Marcin; Tamura, Naoyuki; Akiyama, Masayuki; Aoki, Kentaro 2009, *ApJ*, 693, 507Y
- Yamada, Sanae F.; Sasaki, Shunji S.; Sumiya, Ryoko; Umeda, Kazuyoshi; Shioya, Yasuhiro; Ajiki, Masaru; Nagao, Tohru; Murayama, Takashi; Taniguchi, Yoshiaki 2005, *PASJ*, 57,881Y
- York, Donald G. et al 2000, *AJ*, 120, 1579